

A new quasi-one-dimensional superconductor parent compound NaMn_6Bi_5 with lower antiferromagnetic transition temperatures

Ying Zhou^{1,2,#}, Long Chen^{1,2,#}, Gang Wang^{*,1,2,4}, Yuxin Wang^{1,2}, Zhichuan Wang^{1,2},
Congcong Chai^{1,2}, Zhongnan Guo³, Jiangping Hu^{*,1,2,4}, Xiaolong Chen^{*,1,2,4}

¹ Beijing National Laboratory for Condensed Matter Physics, Institute of Physics, Chinese Academy of Sciences, Beijing 100190, China

² University of Chinese Academy of Sciences, Beijing 100049, China

³ Department of Chemistry, School of Chemistry and Biological Engineering, University of Science and Technology Beijing, Beijing 100083, China

⁴ Songshan Lake Materials Laboratory, Dongguan, Guangdong 523808, China

These authors contributed equally to this work.

*Corresponding author: gangwang@iphy.ac.cn; jphu@iphy.ac.cn; xlchen@iphy.ac.cn;

Keywords: superconductor, quasi-one-dimensional, antiferromagnetic transition

Abstract: Mn-based superconductor is rare and recently reported in quasi-one-dimensional KMn_6Bi_5 with $[\text{Mn}_6\text{Bi}_5]^-$ columns under high pressure. Here we report the synthesis, magnetic properties, electrical resistivity, and specific heat capacity of the newly-discovered quasi-one-dimensional NaMn_6Bi_5 single crystal. Compared with other AMn_6Bi_5 ($A = \text{K}, \text{Rb}, \text{and Cs}$), NaMn_6Bi_5 has larger intra-column Bi-Bi bond length, which may result in the two decoupled antiferromagnetic transitions at 47.3 K and 52.3 K. The relatively lower antiferromagnetic transition temperatures make NaMn_6Bi_5 a more suitable platform to explore Mn-based superconductors. Anisotropic resistivity and non-Fermi liquid behavior at low temperature are observed. Heat capacity measurement reveals that NaMn_6Bi_5 has similar Debye temperature with those of AMn_6Bi_5 ($A = \text{K}$ and Rb), whereas the Sommerfeld coefficient is unusually large. Using first-principles calculations, the quite different density of states and an unusual enhancement near the Fermi level are observed for NaMn_6Bi_5 , when compared with those of other AMn_6Bi_5 ($A = \text{K}, \text{Rb}, \text{and Cs}$) compounds.

1 Introduction

Finding unconventional superconductors violating the Bardeen-Cooper-Schrieffer (BCS) theory is a promising routine to reach room-temperature superconductivity under ambient pressure and brings out fruitful results in the past decades, like cuprates [1, 2], iron pnictides [3, 4] and heavy-fermion superconductors [5, 6]. Apart from the cuprates and iron pnictides, other $3d$ -transition-metal-based compounds are also of great interest in exploring superconductors for their varying coordination environment of $3d$ transition metal [7, 8] and unique magnetism [9, 10]. By suppressing the magnetism of $3d$ -transition-metal-based compounds, unconventional superconductivity is expected to be observed in the vicinity of antiferromagnetic quantum critical point (QCP). However, up to now, only a few $3d$ -transition-metal-based superconductors, such as Cr-based [11-14] or Mn-based [15] superconductors, are reported.

Mn-based superconductor was first reported in three-dimensional MnP with its helical magnetic order suppressed under pressure [15], which suggests that superconductivity could emerge in Mn-based system by suppressing the helical magnetic order. In our former work, an interesting helical magnetic order was predicted in RbMn_6Bi_5 [16], which is a quasi-one-dimensional ternary Mn-based compounds with unique $[\text{Mn}_6\text{Bi}_5]$ -columns similar to KMn_6Bi_5 [17]. Following RbMn_6Bi_5 , we then substituted Rb by smaller alkali metal Na and synthesized NaMn_6Bi_5 having lower antiferromagnetic transition temperatures. Very recently, J. G. Cheng, et al. has reported a pressure-induced superconductivity with transition temperature up to 9.3 K in KMn_6Bi_5 by suppressing the antiferromagnetic order [18], which may open a new avenue for finding more Mn-based superconductors. Considering the even lower antiferromagnetic transition temperatures of NaMn_6Bi_5 than that of KMn_6Bi_5 , we believe that NaMn_6Bi_5 is a more suitable platform to explore superconductivity and other possible exotic properties. Here, the single crystal growth, magnetism, and transport properties of NaMn_6Bi_5 are reported. For the smaller radius of Na, NaMn_6Bi_5 shares a same quasi-one-dimensional structure motif as that of KMn_6Bi_5 and RbMn_6Bi_5 , but having an unusual enhancement of intra-column Bi-Bi bonds. The suppression of antiferromagnetic transition is confirmed by magnetic susceptibility, specific heat capacity, and resistivity measurements. Meanwhile,

anisotropic resistivity, non-Fermi liquid behavior, and largely enhanced Sommerfeld coefficient are observed. First-principles calculations reveal a quite different density of states (DOS) near the Fermi level for NaMn₆Bi₅ compared with those of other AMn₆Bi₅ (A = K, Rb, and Cs). These results demonstrate that NaMn₆Bi₅ is a more promising candidate to explore Mn-based superconductor.

2 Experimental Methods

Single Crystal Growth. NaMn₆Bi₅ single crystals were grown by a high-temperature solution method modified from that reported in our former work [16]. Na chunk (99.75%, Alfa Aesar), Mn powder (99.95%, Alfa Aesar), and Bi granules (99.999%, Sinopharm) were mixed using a molar ratio of Na : Mn : Bi = 0.5 : 4 : 8 in a fritted alumina crucible set (Canfield crucible set) [19] and sealed in a fused-silica ampoule at vacuum. The ampoule was heated to 1073 K over 15 h, held at the temperature for 24 h, and then slowly cooled down to 673 K at a rate of 2 K/h. At 673 K, the single crystals with size up to 5 mm × 0.5 mm × 0.5 mm were separated from the remaining liquids by centrifuging the ampoule. The obtained single crystals are shiny-silver needles and air-sensitive, so all manipulations and specimen preparation for structure characterization and property measurements were handled in an argon-filled glovebox. In addition, CsMn₆Bi₅ single crystals were also grown by using the similar method.

Structure Characterization and Composition Analysis. X-ray diffraction data were obtained using a PANalytical X'Pert PRO diffractometer (Cu K_{α} radiation, $\lambda = 1.54059 \text{ \AA}$) operated at 40 kV voltage and 40 mA current with a graphite monochromator in a reflection mode ($2\theta = 5^{\circ} - 100^{\circ}$, step size = 0.017°). Indexing and Rietveld refinement were performed using the DICVOL91 and FULLPROF programs [20]. Single crystal X-ray diffraction (SCXRD) data were collected using a Bruker D8 VENTURE with Mo K_{α} radiation ($\lambda = 0.71073 \text{ \AA}$) at 300 K. The morphology and analyses of elements were characterized using a scanning electron microscope (SEM, Hitachi S-4800) equipped with an electron microprobe analyzer for semiquantitative elemental analysis in energy-dispersive spectroscopy (EDS) mode, combining with the inductively coupled plasma-atomic emission spectrometer (ICP-AES, Teledyne Leeman Laboratories Prodigy 7).

Five spots in different areas were measured on one crystal using EDS and the ICP-AES measurement was performed on two pieces of single crystal. The crystal structure and chemical composition of CsMn₆Bi₅ single crystal have also been determined.

Physical Property Measurements. The magnetic susceptibility, resistivity, and heat capacity measurements were carried out using a physical property measurement system (PPMS, Quantum Design). Magnetic susceptibility was measured under a small magnetic field (0.1 T) parallel ($H // \text{rod}$) and perpendicular ($H \perp \text{rod}$) to the rod ([010] direction) using the zero-field-cooling (ZFC) and field-cooling (FC) protocols as reported in RbMn₆Bi₅ [16]. For larger fields at 1 T, 2 T, 3 T, 5 T, and 7 T, only magnetic susceptibility in FC protocol was measured. Magnetization hysteresis loops at 5 K, 10 K, 40 K, 50 K, 100 K, and 300 K were measured under the magnetic field up to 7 T parallel and perpendicular to the rod ([010] direction). The resistivity was measured using the standard four-probe configuration with the applied current (about 2 mA) parallel ($I // \text{rod}$) or perpendicular ($I \perp \text{rod}$) to the rod ([010] direction). Heat capacity measurement was carried out below 200 K. To protect the samples from air and moisture, thin film of N-type grease was spread to cover the sample for heat capacity measurement.

First-Principles Calculations. The first-principles calculations were carried out with the projector augmented wave (PAW) method as implemented in the Vienna *ab initio* simulation Package (VASP) [21, 22]. The generalized gradient approximation (GGA) [23] of the Perdew-Burke-Ernzerhof (PBE) [24] type was adopted for the exchange-correlation function. The cutoff energy of the plane-wave basis was 520 eV and the energy convergence standard was set to 10^{-6} eV. The $4 \times 4 \times 4$ and $2 \times 10 \times 4$ Monkhorst-Pack K-point meshes were employed for the Brillouin zone (BZ) sampling of the unit cell and the conventional cell, respectively.

3 Result and Discussion

Crystal Structure.

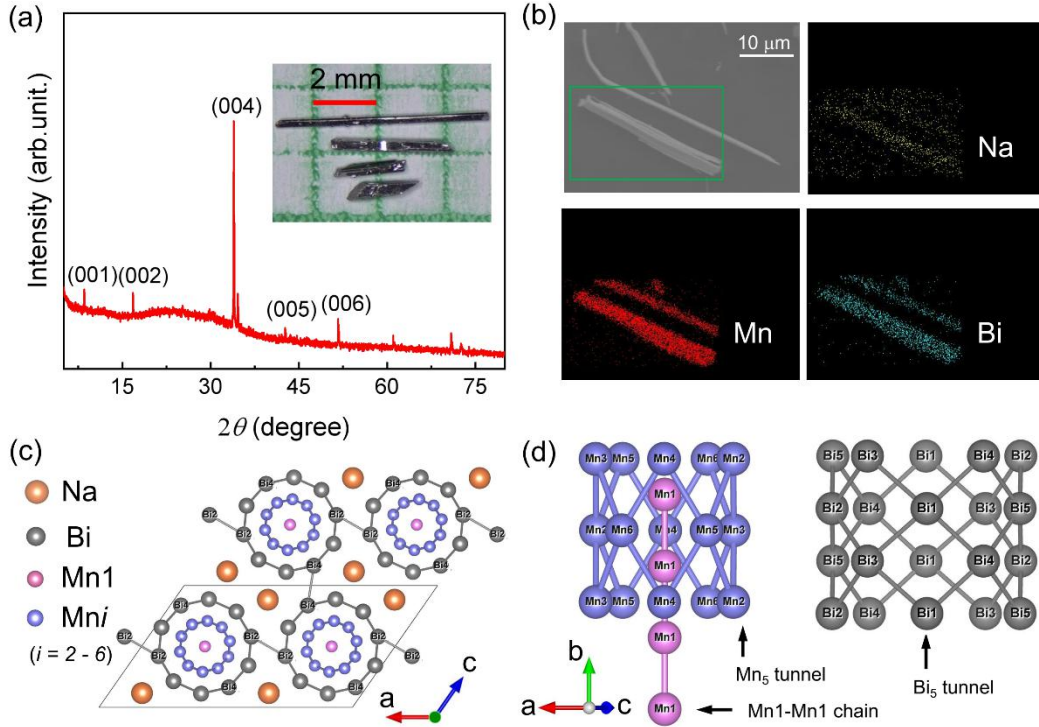


Fig. 1 (a) X-ray diffraction pattern of an as-grown NaMn_6Bi_5 single crystal, showing $(00l)$ reflections. The inset is the optical photograph of NaMn_6Bi_5 single crystals. (b) SEM image of NaMn_6Bi_5 and elemental mapping. (c) Crystal structure of NaMn_6Bi_5 viewed along b axis with inter-column bonds Bi2-Bi2 and Bi4-Bi4 labeled. (d) Crystal structure of Mn_5 tunnel with one-dimensional Mn1-Mn1 chain at the center and Bi_5 tunnel viewed perpendicular to ab plane.

As shown in the inset of Fig. 1a, the as-grown single crystals of NaMn_6Bi_5 are needle-like rods with shiny metal luster, indicating a clear quasi-one-dimensional feature. The X-ray diffraction pattern of an as-grown crystal is plotted in Fig. 1a with a strong preferential orientation of $(00l)$ ($l = \text{integer}$) reflections. Based on the position ($\sim 8.2^\circ$) of (001) diffraction peak, the distance between corresponding structural units was determined to be 12.6 \AA , which is close to the lattice parameter c as reported in KMn_6Bi_5 and RbMn_6Bi_5 [16, 17]. Elemental mapping of NaMn_6Bi_5 (Fig. 1b) confirms the homogeneous distribution of Na, Mn, and Bi. According to EDS (Fig. S1), the molar ratio is close to $\text{Na} : \text{Mn} : \text{Bi} = 1 : 6.37(2) : 5.22(3)$, whereas ICP-AES indicates an molar ratio of $\text{Na} : \text{Mn} : \text{Bi} = 1.008(2) : 6.000(1) : 4.967(2)$. Considering its quasi-one-dimensional feature, we tried to mechanically exfoliate the crystals using the Scotch-tape

method and obtained NaMn₆Bi₅ wires with diameters down to 528 nm (Fig. S1), showing more possibilities in applications.

The determined crystal structure based on the SCXRD data is shown in Fig. 1c and 1d. NaMn₆Bi₅ crystallizes in a monoclinic space group (Table S1) *C2/m* (No. 11) with $a = 22.4357(25)$ Å, $b = 4.5952(5)$ Å, $c = 12.6577(13)$ Å, $\alpha = \gamma = 90^\circ$, and $\beta = 123.109(3)^\circ$. As shown in Fig. 1c, NaMn₆Bi₅ shares a same quasi-one-dimensional structure motif with that of KMn₆Bi₅ [17] and RbMn₆Bi₅ [17], featuring [Mn₆Bi₅]⁻¹ columns extending along the [010] direction, which is surrounded by the counter cation Na⁺ acting as separators. The [Mn₆Bi₅]⁻¹ column is consisted of the Mn₅ tunnel built by Mni ($i = 2-6$) with an inner one-dimensional Mn1-Mn1 atomic chain and the outmost Bi₅ tunnel.

Table I. Lattice parameters and typical bond lengths of AMn₆Bi₅ (A = Na, K, Rb, and Cs).

A	Na	K [17]	Rb [16]	Cs
Radius (pm)	102	138	152	167
a (Å)	22.4357(25)	22.994(2)	23.286(5)	23.6338(14)
b (Å)	4.5952(5)	4.6128(3)	4.6215(9)	4.6189(3)
c (Å)	12.6577(13)	13.3830(13)	13.631(3)	13.8948(8)
α, γ (°)	90	90	90	90
β (°)	123.1092(34)	124.578(6)	125.00(3)	125.447(2)
Bi1-Bi3 (Å)	3.5887	3.52	3.4931	3.4714
Bi1-Bi4 (Å)	3.6277	3.6115	3.6113	3.6015
Bi2-Bi2 (Å)	3.6358	3.5687	3.6061	3.6812
Bi2-Bi4 (Å)	3.5592	3.6517	3.7030	3.7698

The lattice parameters and typical bond lengths of AMn₆Bi₅ (A = Na, K, Rb, and Cs) are summarized in Table I. With the increasing cation radius from Na⁺ (~102 pm) to K⁺ (~138 pm), then to Rb⁺ (~152 pm), and finally to Cs⁺ (~167 pm), the lattice parameters a , b , c , and β all show a monotonic increase. Compared with RbMn₆Bi₅, NaMn₆Bi₅ shows

the shrinkage of a and c as large as 3.65% and 7.14%, respectively, whereas that of b is only 0.57%. Such difference can be interpreted by the strong bonds of Mn-Mn and Bi-Bi along b axis and the much weaker inter-column Na-Bi bonds. The decrease of β suggests potential glides of $[\text{Mn}_6\text{Bi}_5]^{-1}$ columns along a or c axis, which means AMn_6Bi_5 ($A = \text{Na}, \text{K}, \text{Rb}, \text{and Cs}$) could be tuned under stress or pressure. Among all the bonds, the typical intra-column bond length monotonically decreases with increasing cation radius, from 3.5887 Å (Na) to 3.4931 Å (Cs) for Bi1-Bi3 and from 3.6277 Å (Na) to 3.6113 Å (Cs) for Bi1-Bi4, respectively. By contrast, the inter-column bond (Bi4-Bi4) monotonically increases from 3.5592 Å (Na) to 3.7698 Å (Cs) as cation radius increases, whereas another inter-column bond (Bi2-Bi2) shows an anomaly enhancement for NaMn_6Bi_5 , with the relation 3.5687 Å (K) < 3.6061 Å (Rb) < 3.6358 Å (Na) < 3.6812 Å (Cs). The anomaly should be related with the unusual properties of NaMn_6Bi_5 (see below).

Magnetic Property.

Fig. 2a and 2b show the ZFC and FC magnetic susceptibility of NaMn_6Bi_5 single crystals under 0.1 T with $H // \text{rod}$ and $H \perp \text{rod}$ ([010] direction), respectively. The insets of Fig. 2a and 2b show the $d\chi T/dT$ curves, donating the magnetic transition temperatures. For $H // \text{rod}$, the ZFC and FC curves coincide with each other in the entire measured temperature range (2 K - 120 K), showing two AFM transitions at 45.3 K and 50.9 K. For $H \perp \text{rod}$, a small deviation is observed in the AFM transitions. The bifurcation of ZFC and FC curves can be attributed to the magnetic anisotropy [25]. Compared with transition temperatures of KMn_6Bi_5 (~75 K) [17] and RbMn_6Bi_5 (~80 K) [16], the AFM transition is largely suppressed in NaMn_6Bi_5 . Moreover, the AFM transition splits. As predicted in RbMn_6Bi_5 , the moments of Mn1 at the center couple with the moments of Mn_i ($i = 2-6$) at the pentagon, inducing a helical magnetic structure with one magnetic transition temperature [16]. Once these two kinds of moments are decoupled, multiple AFM transitions are expected. The observed lower AFM transition temperatures and split AFM transitions may be the hint of such decoupling, whereas the underline mechanism still remains uncovered. More importantly, the lower AFM transition temperature makes NaMn_6Bi_5 a more promising candidate to explore Mn-based superconductor by chemical doping or applying physical pressure.

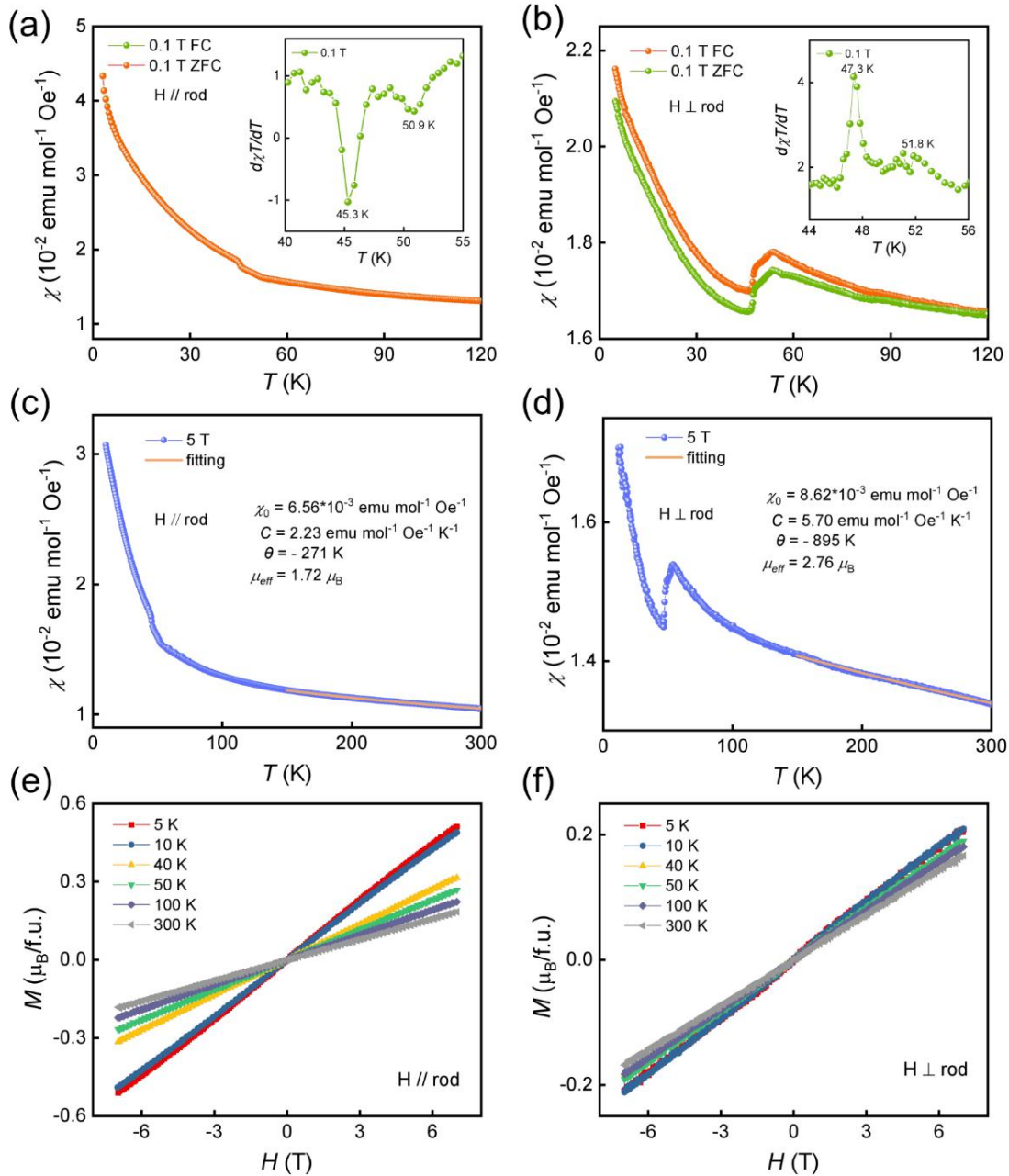


Fig. 2 ZFC and FC magnetic susceptibility of NaMn₆Bi₅ single crystals under 0.1 T for (a) $H // \text{rod}$ and (b) $H \perp \text{rod}$ ([010] direction). The insets are the corresponding $d\chi/dT$ curves. Temperature dependent magnetic susceptibility of NaMn₆Bi₅ single crystals under 5 T for (c) $H // \text{rod}$ and (d) $H \perp \text{rod}$ and corresponding Curie-Weiss fittings from 150 K to 300 K. Field dependent magnetizations for (e) $H // \text{rod}$ and (f) $H \perp \text{rod}$ at different temperatures.

By fitting the magnetic susceptibility under 5 T at high temperature range (150 K-300 K) using Curie-Weiss law, $\chi = \chi_0 + \frac{C}{T-\theta}$, where χ_0 is the temperature-independent contribution including the diamagnetic contribution of the orbital magnetic moment and the Pauli paramagnetic contribution of conduction electron, C is the Curie constant, and θ is the Curie temperature [26]. The fitted values are $\chi_0 = 6.56 \times 10^{-3} \text{ emu mol}^{-1} \text{ Oe}^{-1}$, $\theta = -271 \text{ K}$, and $C = 2.23 \text{ emu mol}^{-1} \text{ Oe}^{-1} \text{ K}^{-1}$ for $H // \text{rod}$, whereas $\chi_0 = 8.62 \times 10^{-3} \text{ emu mol}^{-1} \text{ Oe}^{-1}$, $\theta = -895 \text{ K}$, and $C = 5.70 \text{ emu mol}^{-1} \text{ Oe}^{-1} \text{ K}^{-1}$ for $H \perp \text{rod}$. Negative θ indicates that the interactions in both directions are of AFM character. The frustration factors $|\theta/T_N|$ [27] are calculated to be ~ 6 for $H // \text{rod}$ and ~ 18 for $H \perp \text{rod}$, indicating an anisotropic frustration. This may be attributed to the quite large magnetic anisotropy resulted from the geometry of the quasi-one-dimensional motif.

The effective moment can be derived following the equation $\mu_{eff} = \sqrt{\frac{8C}{n}}$, where n is the number of magnetic atoms. For NaMn_6Bi_5 , the effective moment is $\mu_{eff} \sim 1.72 \mu_B/\text{Mn}$ for $H // \text{rod}$ and $\mu_{eff} \sim 2.76 \mu_B/\text{Mn}$ for $H \perp \text{rod}$, respectively. As discussed in RbMn_6Bi_5 [16], these values fall in the range of the spin-only magnetic moment of low-spin $t_{2g}^{4.67}$ ($1.38 \mu_B$) and high-spin $t_{2g}^3 e_g^{1.67}$ ($5.48 \mu_B$) of octahedrally coordinated $d^{4.67}$, corresponding to the Zintl phase [28] with an average oxidation state of $\text{Mn}^{2.33+}$. The magnetic anisotropy in NaMn_6Bi_5 is larger than that of KMn_6Bi_5 , which maybe be attributed to the effect of cation radius.

The magnetization of NaMn_6Bi_5 under magnetic field parallel and perpendicular to the rod ([010] direction) are shown in Fig. 2e and 2f, respectively. All magnetization curves increase linearly with magnetic field ranging from 5 K to 300 K and remain unsaturated up to 7 T with no hysteresis loop in both directions. The absence of hysteresis in M-H curves confirms the dominant AFM interaction at low temperatures, same as in KMn_6Bi_5 [17] and RbMn_6Bi_5 [16]. By increasing the magnetic field from 1 T to 7 T for $H // \text{rod}$, the two AFM transition temperatures hardly change (Fig. S2), showing the Mn moments in NaMn_6Bi_5 having large saturation magnetic field.

Resistivity.

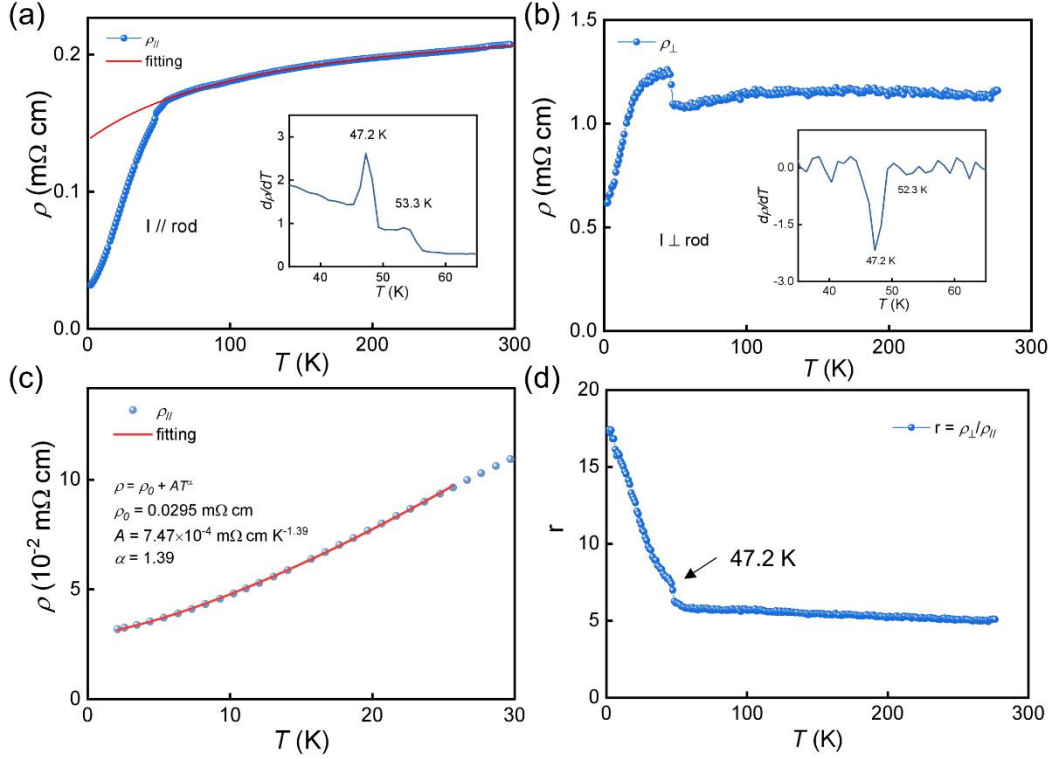


Fig. 3 Temperature dependent resistivity $\rho(T)$ for NaMn_6Bi_5 single crystal measured with (a) $I // \text{rod}$ and (b) $I \perp \text{rod}$ ($[010]$ direction). The insets are the first derivative in the temperature range 35 K - 65 K. (c) The enlarged low-temperature resistivity with $I // \text{rod}$. (d) Temperature dependent anisotropic resistivity ratio for NaMn_6Bi_5 single crystal.

With $I // \text{rod}$, the resistivity of NaMn_6Bi_5 decreases with decreasing temperature, showing a metallic-like behavior with an anomaly around 50 K (Fig. 3a). From the first derivative curve ($d\rho/dT$), two transition temperatures at 47.2 K and 53.3 K can be extracted and coincide with AFM transition temperatures observed in the magnetic susceptibility, which are both direction-independent (Fig. 3b) and sample-independent (Fig. S3). The room-temperature resistivity for NaMn_6Bi_5 is estimated to be 0.207 m Ω cm in the $[010]$ direction, smaller than the maximum value (1 m Ω cm) determined by the MIR limit [29]. The residual resistivity ratio $\text{RRR} = \frac{\rho(300 \text{ K})}{\rho(2 \text{ K})} = 6.5$ indicates that the crystalline quality of NaMn_6Bi_5 is good. Above 55 K, the resistivity can be fitted (red line in Fig. 3a) using the formula $\frac{1}{\rho(T)} = \frac{1}{\rho_{\text{sat}}} + \frac{1}{\rho_{\text{ideal}}}$, where ρ_{sat} represents the saturation

resistivity, ρ_{ideal} is the ideal resistivity that satisfies the Boltzmann equation. ρ_{ideal} is proportional to the temperature in the high temperature region and can be described by $\rho_{\text{ideal}} = \rho_r + aT$ [29]. The fitting yields $\rho_{\text{sat}} = 0.24 \text{ m}\Omega \text{ cm}$, $\rho_r = 0.33 \text{ m}\Omega \text{ cm}$, and $a = 4.4 \times 10^{-3} \text{ m}\Omega \text{ cm K}^{-1}$. As shown in Fig. 4c, the resistivity can be well fitted using $\rho = \rho_0 + AT^\alpha$ below 25 K, with fitted parameters $\rho_0 = 0.0295 \text{ m}\Omega \text{ cm}$, $A = 7.47 \times 10^{-4} \text{ m}\Omega \text{ cm K}^{-1.39}$, and $\alpha = 1.39$. The value of power α deviates largely from 2, suggesting a non-Fermi liquid behavior of NaMn_6Bi_5 at low temperature, which is quite different from the Fermi liquid behavior reported in both KMn_6Bi_5 ($\alpha \sim 2$) [17] and RbMn_6Bi_5 ($\alpha = 1.9$) [16].

In comparison, temperature dependent resistivity with $I \perp$ rod shows an increase below the AFM transition temperature (Fig. 3b). After reaching the maximum, the resistivity begins to decrease again with the decreasing temperature. Similar to that in KMn_6Bi_5 and RbMn_6Bi_5 , the jump is attributed to a dimensional crossover of electrons in low-dimensional materials [16, 17, 30]. The anisotropic resistivity ratio, denoted as $r = \rho_{\perp} / \rho_{\parallel}$, increases with decreasing temperature and sharply increases below the AFM transition temperature (Fig. 3d). The value of anisotropic resistivity ratio is about 17 at 2 K, comparable to that of KMn_6Bi_5 (~ 20) [17] but much smaller than that of RbMn_6Bi_5 (~ 240) [16].

Specific Heat Capacity.

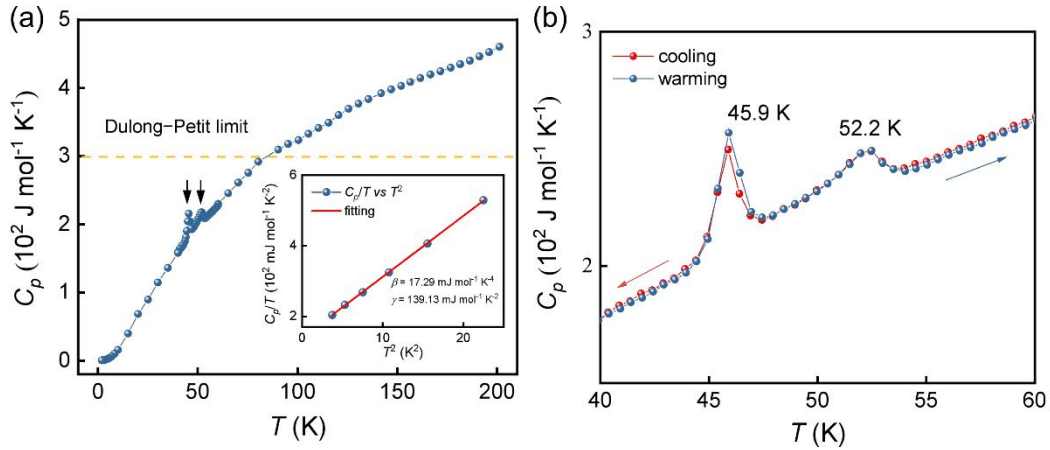


Fig. 4 (a) Temperature dependent specific heat capacity for NaMn_6Bi_5 single crystal. The inset shows the C_p/T versus T^2 , the red solid line is the linear fitting by using Debye

model. (b) The enlarged specific heat capacity around 50 K for cooling down and warming up.

Temperature dependent specific heat capacity for NaMn₆Bi₅ single crystal measuring from 2 K to 200 K is shown in Fig. 4a, which exhibits two peaks at 45.9 K and 52.2 K. These temperatures are close to the transition temperatures of magnetic susceptibility and resistivity, which are sample-independent and reversible for cooling down and warming up (Fig. 4b). The specific heat capacity exceeds the Dulong–Petit limit ($3NR \sim 300 \text{ J mol}^{-1} \text{ K}^{-1}$, yellow dash line) at high temperature, which is also attributed to more prominent phonon contribution at higher temperature of N-type grease used for protecting the sample [16, 17]. For NaMn₆Bi₅, both jumps $\Delta C \sim 28 \text{ J mol}^{-1} \text{ K}^{-1}$ and $11 \text{ J mol}^{-1} \text{ K}^{-1}$ are much smaller than that of RbMn₆Bi₅ ($\Delta C \sim 175 \text{ J mol}^{-1} \text{ K}^{-1}$) and KMn₆Bi₅ ($\Delta C \sim 180 \text{ J mol}^{-1} \text{ K}^{-1}$). We then fit the low-temperature (2 K - 5 K) specific heat capacity with Debye model $C = \gamma T + \beta T^3$, where γT represents the contribution from the electron, βT^3 represents the contribution of the lattice. The Sommerfeld coefficient γ proportional to the DOS at the Fermi level is determined to be 139.13 mJ K^{-2} per formula [$23.2 \text{ mJ K}^{-2} (\text{mol-Mn})^{-1}$], much larger (3~5 times) than that of RbMn₆Bi₅ (28.2 mJ K^{-2} per formula) [16] and KMn₆Bi₅ (39.0 mJ K^{-2} per formula) [17]. This indicates the decreasing trend of DOS at the Fermi level by increasing the cation radius from Na to Rb, which is also held for other quasi-one-dimensional materials like A₂Cr₃As₃ (A = K, Rb, and Cs) [12-14] with the underlying mechanism unknown. The Debye temperature Θ_D can be calculated by $(12\pi^4 Rn/5\beta)^{1/3}$, where R represents the molar gas constant and n is the number of atoms in the chemical formula. For NaMn₆Bi₅, the Debye temperature Θ_D is 110.8 K, quiet close to that of RbMn₆Bi₅ (107.8 K) [16] and KMn₆Bi₅ (114.6 K) [17], which can be attributed to the quite similar crystal structure of these compounds.

Density of States.

We then tried to understand the effect of structure anomaly in NaMn₆Bi₅ and the origin of its different magnetic transitions, non-Fermi liquid behavior, and much enhanced Sommerfeld coefficient by calculating DOS near the Fermi level for AMn₆Bi₅ (A = Na, K, Rb, and Cs) using first-principles calculations. As shown in Fig. 5, all AMn₆Bi₅ (A = Na, K, Rb, and Cs) compounds have non-zero DOS at Fermi level (E_F),

corresponding well with the observed metallic-like behavior in resistivity. Compared with other AMn_6Bi_5 ($A = K, Rb,$ and Cs) compounds, $NaMn_6Bi_5$ shows a quite different DOS near the Fermi level (E_F), which may correspond to those different characteristics. Specially, a peak and a larger dip (red arrows) emerge around E_F in $NaMn_6Bi_5$, which should be responsible for the much enhanced Sommerfeld coefficient.

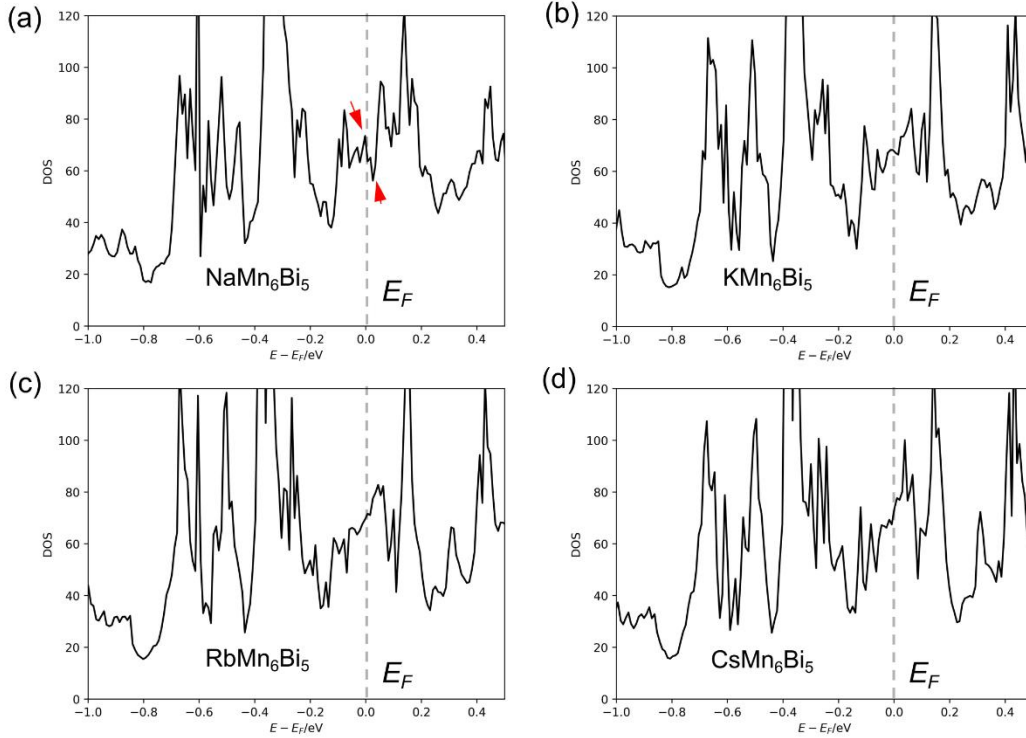


Fig. 5 DOS near the Fermi level (E_F , dash lines) from -1 eV to 0.5 eV for (a) $NaMn_6Bi_5$, (b) KMn_6Bi_5 , (c) $RbMn_6Bi_5$, and (d) $CsMn_6Bi_5$. Red arrows donate the difference of DOS for $NaMn_6Bi_5$ around E_F compared with other AMn_6Bi_5 ($A = K, Rb,$ and Cs) compounds.

4 Conclusion

In conclusion, a new quasi-one-dimensional superconductor parent compound $NaMn_6Bi_5$ has been discovered. Compared with other AMn_6Bi_5 ($A = K, Rb,$ and Cs), $NaMn_6Bi_5$ has a larger intra-column Bi-Bi bond length. This structure anomaly may result in the two decoupled AFM transitions at 47.3 K and 51.8 K observed in magnetic susceptibility, resistivity, and heat capacity measurements. Anisotropic resistivity, non-Fermi liquid behavior, and much enhanced Sommerfeld coefficient are observed, which

may be attributed to the different DOS near the Fermi level compared with other AMn_6Bi_5 ($A = \text{K}, \text{Rb}, \text{and Cs}$) compounds. The decoupled AFM transitions and lower AFM transition temperatures make NaMn_6Bi_5 a more promising platform for exploring the exchange-coupling interaction and superconductivity. Chemical doping and physical pressure should be the effective means to induce superconductivity within such quasi-one-dimensional materials with possible helical magnetic order.

Supporting information

Table S1 compares the crystal structure of NaMn_6Bi_5 and CsMn_6Bi_5 . Figure S1 displays the quasi-one-dimensional feature of NaMn_6Bi_5 . Figure S2 shows the magnetic susceptibility of NaMn_6Bi_5 single crystal under various magnetic field. Figure S3-S4 are temperature dependent resistivity and specific heat capacity of other NaMn_6Bi_5 single crystals, respectively.

Author information

Notes

The authors declare no competing financial interest.

Acknowledgements

This work was partially supported by the National Key Research and Development Program of China (Grant Nos. 2017YFA0302902 and 2018YFE0202600), the National Natural Science Foundation of China (Grant No. 51832010), , and the Key Research Program of Frontier Sciences, Chinese Academy of Sciences (Grant No. QYZDJ-SSW-SLH013).

References

- [1] J. G. Bednorz, K. A. Müller, Possible high T_c superconductivity in the Ba–La–Cu–O system, *Z. Phys. B: Condens. Matter* 64, 189 (1986).
- [2] P. A. Lee, N. Nagaosa, X. G. Wen, Doping a Mott insulator: Physics of high-temperature superconductivity, *Rev. Mod. Phys.* 78, 17 (2006).
- [3] Y. Kamihara, H. Hiramatsu, M. Hirano, R. Kawamura, H. Yanagi, T. Kamiya, H. Hosono, Iron-based layered superconductor: LaOFeP, *J. Am. Chem. Soc.* 128, 10012 (2006).
- [4] Y. Kamihara, T. Watanabe, M. Hirano, H. Hosono, Iron-based layered superconductor La[O_{1-x}F_x]FeAs ($x = 0.05$ – 0.12) with $T_c = 26$ K, *J. Am. Chem. Soc.* 130, 3296 (2008).
- [5] F. Steglich, J. Aarts, C. D. Bredl, W. Lieke, D. Meschede, W. Franz, H. Schäfer, Superconductivity in the presence of strong pauli paramagnetism: CeCu₂Si₂, *Phys. Rev. Lett.* 43, 1892 (1979).
- [6] G. R. Stewart, Heavy-fermion systems, *Rev. Mod. Phys.* 56, 755 (1984).
- [7] P. L. Alireza, Y. C. Ko, J. Gillett, C. M. Petrone, J. M. Cole, G. G. Lonzarich, S. E. Sebastian, Superconductivity up to 29 K in SrFe₂As₂ and BaFe₂As₂ at high pressures, *J. Phys. Condens. Mat.* 21, 012208 (2008).
- [8] A. Akbari, I. Eremin, P. Thalmeier, RKKY interaction in the spin-density-wave phase of iron-based superconductors, *Phys. Rev. B* 84, 134513 (2011).
- [9] K. Marty, A. D. Christianson, C. H. Wang, M. Matsuda, H. Cao, L. H. VanBebber, J. L. Zarestky, D. J. Singh, A. S. Sefat, M. D. Lumsden, Competing magnetic ground states in nonsuperconducting Ba(Fe_{1-x}Cr_x)₂As₂ as seen via neutron diffraction, *Phys. Rev. B* 83, 060509 (2011).
- [10] L. Chen, C. Cao, H. X. Chen, J. G. Guo, J. Ma, J. P. Hu, G. Wang, Miscibility gap and possible intrinsic Griffiths phase in Sr(Fe_{1-x}Mn_x)₂As₂ crystals grown by transition metal arsenide flux, *Phys. Rev. B* 103, 134509 (2021).
- [11] W. Wu, J. Cheng, K. Matsubayashi, P. Kong, F. Lin, C. Jin, N. Wang, Y. Uwatoko, J. Luo, Superconductivity in the vicinity of antiferromagnetic order in CrAs, *Nat. Commun.* 5, 5508 (2014).
- [12] J. K. Bao, J. Y. Liu, C. W. Ma, Z. H. Meng, Z. T. Tang, Y. L. Sun, H. F. Zhai, H. Jiang, H. Bai, C. M. Feng, Z. A. Xu, G. H. Cao, Superconductivity in quasi-one-dimensional K₂Cr₃As₃ with significant electron correlations, *Phys. Rev. X* 5, 011013 (2015).
- [13] Z. T. Tang, J. K. Bao, Y. Liu, Y. L. Sun, A. Ablimit, H. F. Zhai, H. Jiang, C. M. Feng, Z. A. Xu, G. H. Cao, Unconventional superconductivity in quasi-one-dimensional Rb₂Cr₃As₃, *Phys. Rev. B* 91, 020506 (2015).
- [14] Z. T. Tang, J. K. Bao, Z. Wang, H. Bai, H. Jiang, Y. Liu, H. F. Zhai, C. M. Feng, Z. A. Xu, G. H. Cao, Superconductivity in quasi-one-dimensional Cs₂Cr₃As₃ with large interchain distance, *Sci. China Mater.* 58, 16 (2015).
- [15] M. Matsuda, F. Ye, S. E. Dissanayake, J. G. Cheng, S. Chi, J. Ma, H. D. Zhou, J. Q. Yan, S. Kasamatsu, O. Sugino, T. Kato, K. Matsubayashi, T. Okada, Y. Uwatoko, Pressure dependence of the magnetic ground states in MnP, *Phys. Rev. B* 93, 5 (2016).

- [16] L. Chen, L. L. Zhao, X. L. Qiu, Q. H. Zhang, K. Liu, Q. S. Lin, G. Wang, Quasi-one-dimensional structure and possible helical antiferromagnetism of RbMn_6Bi_5 , *Inorg. Chem.* 60, 12941 (2021).
- [17] J. K. Bao, Z. T. Tang, H. J. Jun, J. Y. Liu, Y. Liu, L. Li, Y. K. Li, Z. A. Xu, C. M. Feng, H. J. Chen, D. Y. Chung, V. P. Dravid, G. H. Cao, M. G. Kanatzidis, Unique Mn_6Bi_5^- nanowires in KMn_6Bi_5 : A quasi-one-dimensional antiferromagnetic metal, *J. Am. Chem. Soc.* 140, 4391 (2018).
- [18] Z. Y. Liu, Q. X. Dong, P. T. Yang, P. F. Shan, B. S. Wang, J. P. Sun, Y. Uwatoko, G. F. Chen, X. L. Dong, Z. X. Zhao, J. G. Cheng, Pressure-induced superconductivity up to 9 K in the quasi-one-dimensional KMn_6Bi_5 , *Arxiv*, 2022.
- [19] P. C. Canfield, T. Kong, U. S. Kaluarachchi, N. H. Jo, Use of frit-disc crucibles for routine and exploratory solution growth of single crystalline samples, *Philos. Mag.* 96, 84 (2016).
- [20] J. Rodríguez-Carvajal, *FullProf*, (CEA/Saclay, France, 2001).
- [21] G. Kresse, J. Hafner, Abinitio molecular-dynamics for liquid-metals, *Phys. Rev. B* 47, 558 (1993).
- [22] G. Kresse, J. Furthmuller, Efficient iterative schemes for ab initio total-energy calculations using a plane-wave basis set, *Phys. Rev. B* 54, 11169 (1996).
- [23] J. P. Perdew, K. Burke, M. Ernzerhof, Generalized gradient approximation made simple (vol 77, pg 3865, 1996), *Phys. Rev. Lett.* 78, 1396 (1997).
- [24] G. Kresse, J. Furthmuller, Efficiency of ab-initio total energy calculations for metals and semiconductors using a plane-wave basis set, *Comput. Mater. Sci.* 6, 15 (1996).
- [25] W. J. Wang, R. Sun, S. J. He, Z. Y. Jia, C. L. Su, Y. Li, Z. C. Wang, Atomic structure, work function and magnetism in layered single crystal VOCl_2 , *2D Mater.* 8, 015027 (2021).
- [26] D. C. Johnston, The puzzle of high temperature superconductivity in layered iron pnictides and chalcogenides, *Adv. Phys.* 59, 803 (2010).
- [27] J. E. Greedan, Geometrically frustrated magnetic materials, *J. Mater. Chem.* 11, 37 (2001).
- [28] R. Nesper, The Zintl-Klemm concept - a historical survey, *Z. Anorg. Allg. Chem.* 640, 2639 (2014).
- [29] O. Gunnarsson, M. Calandra, J. E. Han, Colloquium: Saturation of electrical resistivity, *Rev. Mod. Phys.* 75, 1085 (2003).
- [30] T. Valla, P. D. Johnson, Z. Yusof, B. Wells, Q. Li, S. M. Loureiro, R. J. Cava, M. Mikami, Y. Mori, M. Yoshimura, T. Sasaki, Coherence–incoherence and dimensional crossover in layered strongly correlated metals, *Nature* 417, 627 (2002).

Supporting information

Table S1. Crystal structure of NaMn₆Bi₅ and CsMn₆Bi₅ obtained by structural refinement from single crystal X-ray diffraction data.

Empirical formula	NaMn ₆ Bi ₅	CsMn ₆ Bi ₅
Formula weight	1397.52 g/mol	1507.43 g/mol
Space group / Z	<i>C2/m</i> (No. 12) /4	<i>C2/m</i> (No. 12) /4
Unit cell dimensions	$a = 22.581(6) \text{ \AA}$ $b = 4.6207(13) \text{ \AA}$ $c = 12.754(4) \text{ \AA}$ $\alpha = \gamma = 90^\circ$ $\beta = 123.196(8)^\circ$	$a = 23.6338(14) \text{ \AA}$ $b = 4.6189(3) \text{ \AA}$ $c = 13.8948(8) \text{ \AA}$ $\alpha = \gamma = 90^\circ$ $\beta = 125.447(2)^\circ$
Volume / d_{cal}	1113.6(6) \AA^3 / 8.961 g/cm ³	1235.6(5) \AA^3 / 8.711 g/cm ³
Reflections collected/R(int)	5362 / 0.1418	6427 / 0.079
Data / restraints / parameters	1499 / 0 / 73	1278 / 0 / 73
Final R indices [I > 2sigma(I)]	$R_1 = 0.0615$, $wR_2 = 0.1607$	$R_1 = 0.0512$, $wR_2 = 0.0565$
R indices (all data)	$R_1 = 0.0872$, $wR_2 = 0.1951$	$R_1 = 0.0595$, $wR_2 = 0.0603$
Largest diff. peak and hole	2.010 and -2.491 e. \AA^{-3}	1.010 and -2.132 e. \AA^{-3}

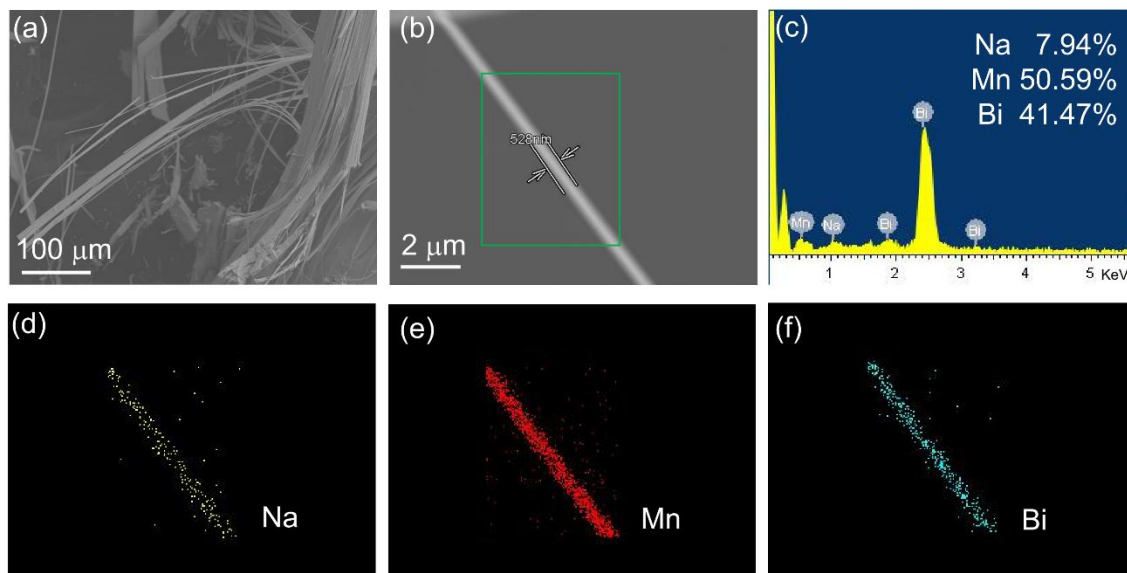


Fig. S1 Quasi-one-dimensional feature of NaMn_6Bi_5 . SEM image of NaMn_6Bi_5 at a scale of (a) $100\ \mu\text{m}$ and (b) $2\ \mu\text{m}$. Elemental analysis (c) and elemental mapping for (d) Na, (e) Mn, and (f) Bi by EDX on the wire.

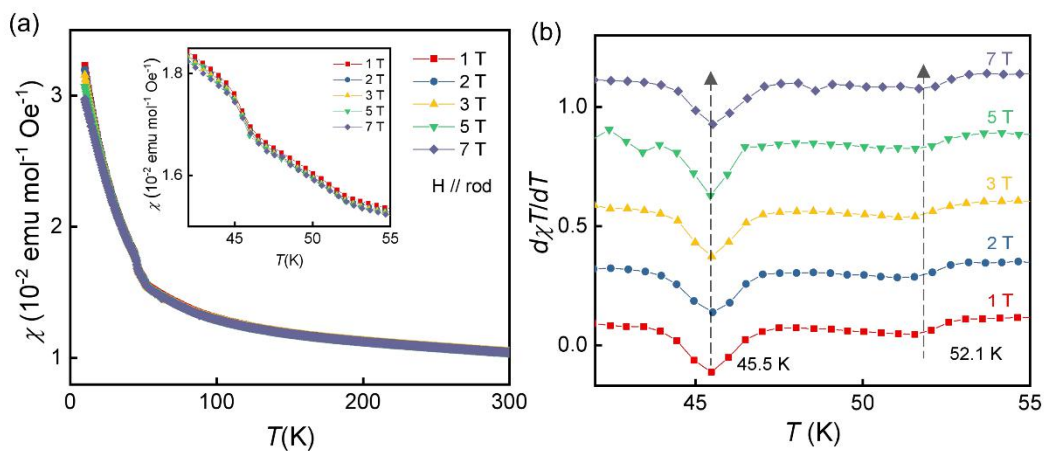


Fig. S2 (a) Temperature dependent magnetic susceptibility of NaMn_6Bi_5 single crystal under various magnetic field for $H // \text{rod}$. The inset is the zoomed susceptibility around 50 K. (b) The $d\chi T/dT$ curves in the temperature range 42 K - 55 K, showing almost unchanged magnetic transition temperatures with increasing magnetic field.

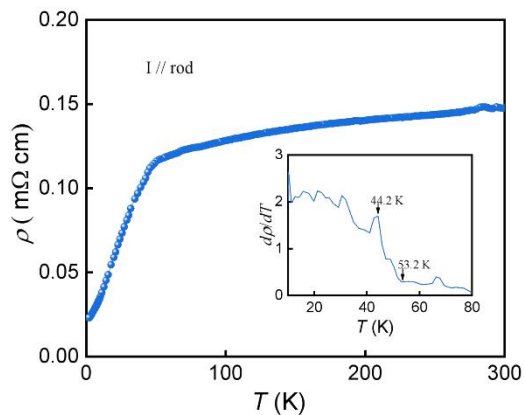


Fig. S3 Temperature dependent resistivity of another NaMn_6Bi_5 single crystal. The inset is the first derivative curve in the temperature range 10 K - 80 K.

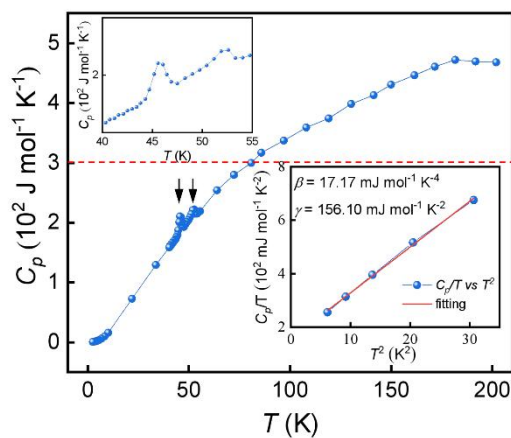


Fig. S4 Temperature dependent specific heat capacity of another NaMn_6Bi_5 single crystal and the corresponding linear fitting at low temperature range by using Debye model.